

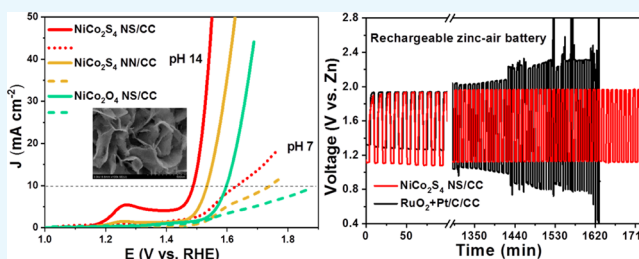
Hierarchical Nickel–Cobalt Dichalcogenide Nanostructure as an Efficient Electrocatalyst for Oxygen Evolution Reaction and a Zn–Air Battery

Suyeon Hyun and Sangaraju Shanmugam*

Department of Energy Science Engineering, Daegu Gyeongbuk Institute of Science & Technology (DGIST), Daegu 42988, The Republic of Korea

Supporting Information

ABSTRACT: A unique three-dimensional (3D) structure consisting of a hierarchical nickel–cobalt dichalcogenide spinel nanostructure is investigated for its electrocatalytic properties at benign neutral and alkaline pH and applied as an air cathode for practical zinc–air batteries. The results show a high oxygen evolution reaction catalytic activity of nickel–cobalt sulfide nanosheet arrays grown on carbon cloth (NiCo_2S_4 NS/CC) over the commercial benchmarking catalyst under both pH conditions. In particular, the NiCo_2S_4 NS/CC air cathode shows high discharge capacity, a narrow potential gap between discharge and charge, and superior cycle durability with reversibility, which exceeds that of commercial precious metal-based electrodes. The excellent performance of NiCo_2S_4 NS/CC in water electrolyzers and zinc–air batteries is mainly due to highly exposed electroactive sites with a rough surface, morphology-based advantages of nanosheet arrays, good adhesion between NiCo_2S_4 and the conducting carbon cloth, and the active layer formed of nickel–cobalt (oxy)hydroxides during water splitting. These results suggest that NiCo_2S_4 NS/CC could be a promising candidate as an efficient electrode for high-performance water electrolyzers and rechargeable zinc–air batteries.



INTRODUCTION

Splitting water into pure hydrogen and oxygen to generate sustainable green hydrogen energy has been intensively studied in recent years, which can replace fossil fuel use.^{1,2} However, the efficiency of water splitting has so far been limited by the lack of sustainable catalysts toward the oxygen evolution reaction (OER) that can accelerate the kinetics.^{3–5} So far, IrO_x and RuO_2 are the best-known OER catalysts, although their high cost and scarcity limit their widespread use.⁴ Meanwhile, some promising attempts have been devoted to developing an efficient nonprecious metal OER catalyst under alkaline conditions. However, an almost harsh alkaline medium presents severe corrosion and related environmental issues.^{6,7} In this regard, someday, the splitting of water at neutral pH from ocean or river would be the target goal to satisfy renewable future hydrogen energy.⁴ It is thus highly required to develop efficient OER electrocatalysts that can operate in both alkaline and neutral media for overall water splitting even though it is relatively tough searching for those catalysts.

Nowadays, various nonprecious transition metal-based catalysts are being explored, for example, transition metals,⁸ transition-metal oxides,^{9,10} chalcogenides,^{11–14} phosphides,^{15–17} hydroxides/oxyhydroxides,^{18,19} carbides,²⁰ borides,²¹ and so on. Although lots of established catalysts have been reported concerning their excellent OER activity under alkaline conditions, only a few of them could still maintain their catalytic activity in neutral media. Cai et al. reported that

the amorphous cobalt sulfide porous nanocubes showed a low OER onset potential of 1.5 V, comparable to that of RuO_2 (1.49 V).²² However, a still substantial overpotential of 570 mV is needed to generate 4.59 mA cm^{-2} in phosphate-buffered solutions (PBSs; pH 7.0), whereas it could generate 10 mA cm^{-2} current density at 290 mV in 1 M KOH (pH 14.0). Similarly, sulfur-incorporated NiFe_2O_4 nanosheets (NSs) on nickel foam (S- NiFe_2O_4 /NF) developed by Liu et al. exhibited a remarkably enhanced water-splitting performance for both OER and hydrogen evolution reaction (HER) as a bifunctional electrode under both alkaline and neutral conditions.²³ The S- NiFe_2O_4 /NF still requires 1.921 V to deliver 10 mA cm^{-2} in 1 M PBS (pH 7.4) for overall water splitting in three electrode systems, mostly occurring during OER with an overpotential of 494 mV. As air cathode catalysts for Zn–air batteries, Prabu et al. demonstrated a highly active one-dimensional structure of a spinel NiCo_2O_4 catalyst in rechargeable Zn–air batteries and Li– O_2 batteries.^{24,26} Recently, Meng et al. constructed $\text{Co}_{0.85}\text{Se}$ nanocrystals in situ coupled with N-doped carbon with a metal–nitrogen–carbon (M–N–C) structure and short diffusion pathways for the transport of electron/ion to improve the Zn–air battery performance.^{25,27} For instance, Wu et al. reported zinc cobalt

Received: June 19, 2018

Accepted: July 20, 2018

Published: August 2, 2018

sulfide, the nanoneedle (NN) arrays grown on the carbon fiber paper electrode catalyst, which enables the Zn–air battery operation with an overpotential of 0.85 V and a long cycle life time of up to 200 cycles at 10 mA cm⁻² as well as comparable water-splitting performance.²⁸ Wang et al. proposed Co₃FeS_{1.5}(OH)₆ hydroxysulfides serving as a superb air electrode catalyst with a low overpotential of 0.84 V and prolonged cyclability over 36 h test for 108 cycles at 2 mA cm⁻².²⁹

In pursuit of high electrochemical performance in water electrolyzers and for a Zn–air battery application, the spinel bimetallic sulfide NiCo₂S₄ with abundant redox chemistry has been considered to be the most promising electrochemically active material, which exhibits 2 orders of magnitude larger than that of NiCo₂O₄ and $\sim 10^4$ times better electric conductivity than conventional single-metal compounds.^{12,30} Moreover, the stable spinel structures of bimetallic sulfide with a formula of AB₂S₄ possess plentiful exposed edge sites, leading to a higher electrochemical activity. Therefore, it has been widely applied for supercapacitors, Li-ion batteries, and a counter electrode for dye-sensitized solar cells as well as in water electrolyzers.³¹ For example, in our group, NiCo₂S₄ nanowire arrays were directly grown on 3D Ni foam (NiCo₂S₄ NW/NF) as a water-splitting catalyst and applied in an alkaline water electrolyzer. Because of its intrinsic properties, large surface area, and well-separated NW structures, NiCo₂S₄ NW/NF afforded continuous water-splitting reaction of generating hydrogen and oxygen gas at a cell voltage of only 1.63 V to generate 10 mA cm⁻² current density.³² Ma et al. developed 3D networked porous NiCo₂S₄ nanoflakes on NF, which can offer more exposed active sites and easy transport of electrons and ions, thereby leading to significantly improved HER activity and stability.³³ The outstanding OER performance of the spinel bimetallic sulfide NiCo₂S₄ has also become a promising application for rechargeable Zn–air batteries involving reversible OER and ORR.

Also, hybridizing NiCo₂S₄ with the 3D structure of NS or NN with a carbon cloth (CC) (NiCo₂S₄ NS/CC or NN/CC) substrate by an in situ growth hydrothermal approach can be an efficient way to enhance the robustness of the electrode. It could also help to minimize the agglomeration of NiCo₂S₄ nanostructures and the detachment during long-term operation, and make faster ion/electron kinetics. Also, the advantages of CC, such as flexibility, high conductivity, and corrosion/dissolution resistivity might lead to enhanced catalytic activity and stability in a wide pH range.³⁴ Meanwhile, tuning the nanostructure and the morphology, as well as porosity, can be another promising strategy to produce numerous exposed catalytic active sites on the catalyst surface.¹⁷

On the basis of our knowledge, we describe the physical and electrochemical properties of NiCo₂S₄ NS/CC as a highly active OER catalyst in both neutral and alkaline media, which have not been thoroughly investigated so far. Mainly, this is the first time a bimetallic sulfide, the NiCo₂S₄-based material, is reported to catalyze OER under a neutral condition. The catalytic performance of NiCo₂S₄ NS/CC is remarkably enhanced compared to the recent reports, particularly under a neutral condition. The NiCo₂S₄ NS/CC electrocatalyst exhibits the lowest OER overpotentials of 260 and 402 mV to generate 10 mA cm⁻² in alkaline and neutral media, respectively. Specifically, it exhibits a low Tafel slope of 123 mV dec⁻¹ and a high turnover frequency (TOF) of 8.17 ×

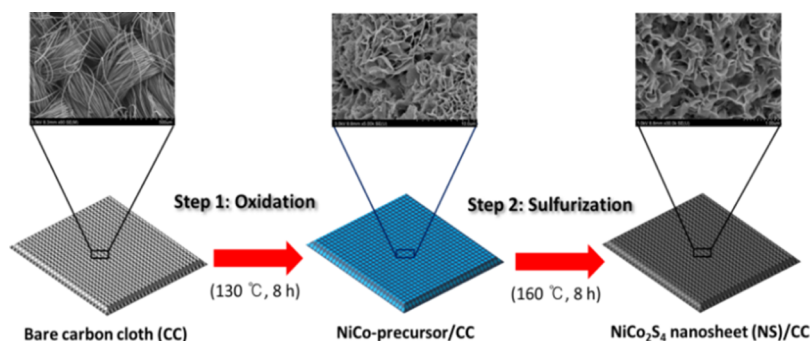
10⁻³ s⁻¹ at 1.63 V applied potential to drive 10 mA cm⁻² current density under neutral conditions, confirming superior intrinsic activity with a substantial electrochemical active surface area (ECSA) of NiCo₂S₄ NS/CC compared with commercial RuO₂/CC and other previously reported OER electrocatalysts. In addition, the constructed NiCo₂S₄ NS/CC air cathode for primary and rechargeable Zn–air batteries exhibits high discharge capacity, a narrow overall overpotential, and a long cycling life time exceeding the benchmark for precious metal-based electrodes.

■ EXPERIMENTAL METHODS

Material Synthesis. Cobalt nitrate hexahydrate [Alfa Aesar, Co(NO₃)₂·6H₂O], nickel nitrate hexahydrate [Sigma-Aldrich, Ni(NO₃)₂·6H₂O], urea (Sigma-Aldrich, CH₄N₂O), and sodium sulfide hydrate (Sigma-Aldrich, Na₂S·xH₂O) were used to synthesize the electrodes. A piece of CC (NARA CELL-TECH, 0.7 cm × 0.7 cm) was utilized with further treatment with ethanol. The NiCo₂S₄ NSs grown on CC (NiCo₂S₄ NS/CC) were prepared through a two-step hydrothermal process. A nickel nitrate of 0.004 M and cobalt nitrate of 0.008 M was dissolved in 120 mL of deionized water; further, 0.012 M urea was added. The obtained solution was transferred into a Teflon-lined stainless steel autoclave of 200 mL capacity, and a piece of CC was immersed in the solution. The autoclave was heated at 120 °C for 8 h in an electric oven. After the first step, the electrode was washed with deionized water several times to eliminate unreacted residues. Consequently, sodium sulfide flakes were dissolved in deionized water to prepare a 0.2 M sulfide solution for a sulfurization process. This sulfur-containing solution was again transferred to the autoclave and heated at 160 °C for 8 h in an electric oven. After cooling down to room temperature naturally, we washed the synthesized electrode several times with ethanol and deionized water, followed by the drying step in the vacuum oven at 60 °C overnight. For comparison, NiCo₂S₄ NN arrays on CC (NiCo₂S₄ NN/CC) were prepared by changing the temperature of the first hydrothermal step from 120 to 130 °C and maintaining the heating time of 8 h. To synthesize NiCo₂O₄ with NSs morphology, which is grown on CC (NiCo₂O₄ NS/CC), the electrode after the first step of the hydrothermal growth process was annealed at 450 °C for 2 h in an air atmosphere.

Microstructural Characterizations. The morphology and element compositions were studied on a field-emission scanning electron microscopy (FE-SEM, Hitachi-S4800, 3 kV) system equipped with a Horiba Scientific energy dispersive spectrometer and using transmission electron microscopy (TEM, Hitachi HF-3300, 300 kV). The crystal structures of all catalysts were examined by powder X-ray diffraction (XRD, Rigaku MiniFlex600). The composition of the catalyst was studied using X-ray photoelectron spectroscopy (XPS, Thermo-Scientific ESCALAB 250Xi).

Electrochemical Measurements. For electrochemical measurements, the OER catalytic performance was evaluated by linear sweep voltammetry (LSV) with a low scan rate of 1 mV s⁻¹ in an electrolyte of 1 M KOH and a PBS without purging oxygen. The OER performance was evaluated in a three-electrode configuration directly using synthesized electrodes such as NiCo₂S₄ NS/CC, NiCo₂S₄ NN/CC, and NiCo₂O₄ NS/CC as a working electrode (1.0 mg cm⁻²), a saturated calomel electrode (SCE) as a reference electrode, and a Pt wire as the counter electrode. Similarly, commercial

Scheme 1. Schematic Preparation Process of Self-Supported NiCo_2S_4 NS/CC Nanostructures

RuO_2 cast onto CC was used as a working electrode (1.4 mg cm^{-2}), Pt wire as a counter electrode, and SCE as a reference electrode. The potentials reported were converted to the reversible hydrogen electrode (RHE). All electrochemical results were iR -corrected, considering the ohmic resistance from the electrolyte. The current densities presented in this paper are normalized concerning the geometric surface area of the electrode. The cyclic voltammetry (CV) was performed in N_2 -saturated 1 M KOH at room temperature with a scan rate of 10 mV s^{-1} . Electrochemical impedance spectroscopy (EIS) was performed within a frequency range of 0.01 Hz to 0.1 MHz.

The ECSA is calculated by following an established methodology reported in the literature.³² In detail, through the cyclic voltammogram obtained in a non-faradaic region at various scan rates (1, 2.5, 5, 10, 20, and 50 mV s^{-1}), double-layer capacitance (C_{dl}) can be estimated. By plotting the anodic and cathodic current densities against the scan rate, the obtained linear slope value is C_{dl} . Finally, the ECSA can be obtained from the following equation:

$$\text{ECSA} = C_{\text{dl}}/C_s$$

C_s denotes the specific capacitance of a flat, smooth surface of the electrode material, which is assumed to be $26 \mu\text{F cm}^{-2}$ for Ni- and Co-containing materials.

Zinc–Air Battery Fabrication and Testing. For full-cell zinc–air battery evaluation, the as-synthesized NiCo_2S_4 NS/CC or commercial catalyst of $\text{RuO}_2 + \text{Pt/C/CC}$ was used as an air-breathing cathode (1.54 cm^2). Typically, the NiCo_2S_4 NS/CC air cathode was prepared with a loading amount of 1.0 mg cm^{-2} . The commercial catalyst-based cathode was fabricated by coating with 2 mg of RuO_2 and 40 wt % Pt/C on CC to achieve a loading of 1.30 mg cm^{-2} . A polished zinc plate with a thickness of 0.1 mm, 6 M KOH solution with 0.2 M zinc acetate, and a Whatman glass microfiber filter membrane were prepared as an anode, an electrolyte, and a separator, respectively, to assemble the zinc–air battery with a coin cell (MTI Korea) configuration. The specific capacity and the charge–discharge curves were reported with a battery analyzer (BST8-3), which consumed ambient air. The discharge capacity of the primary zinc–air cell was normalized to the consumed mass of Zn metal, whereas the current density was normalized to the area of the electrode.

RESULTS AND DISCUSSION

The hierarchical bimetallic sulfide NS arrays/CC hybrids were developed using an in situ two-step hydrothermal method, as graphically represented in Scheme 1. In the first step of the hydrothermal process, nickel nitrate hexahydrate and cobalt

nitrate hexahydrate in a stoichiometric ratio were dissolved in deionized water and then urea was added. The solution was transferred into an autoclave and heated at 120°C for 8 h, forming cobalt–nickel carbonate hydroxide hydrate NS arrays on a CC substrate. Subsequently, after oxidation reaction, a solution of sodium sulfide flakes dissolved in deionized water was prepared for the next sulfurization process. The anion exchange reaction from $\text{Co}_3^{2-}/\text{OH}^-$ anions to S^{2-} anions occurred at 160°C for 6 h, thereby leading the complete phase transformation from cobalt–nickel carbonate hydroxide hydrate to nickel–cobalt sulfide on the CC. The morphology and composition of NiCo_2S_4 NS/CC were studied by FE-SEM and TEM. The bare CC consists of interconnected fibers with a smooth surface, as shown in Figure 1a. After the first hydrothermal reaction, numerous NS arrays are stacked onto the surface of CC with a rough surface shown in Figures 1b and S1. Consequently, the second hydrothermal process for sulfurization treatment is conducted, and its NS-like

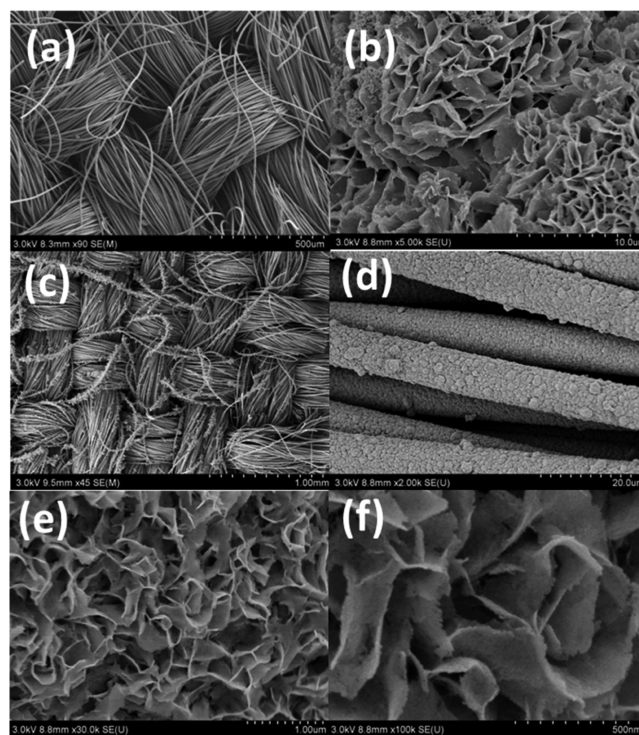


Figure 1. FE-SEM images of (a) bare CC, (b) NiCo-precursor/CC after the first step in the hydrothermal process, (c–f) NiCo_2S_4 NS arrays grown on the surface of CC at different magnifications.

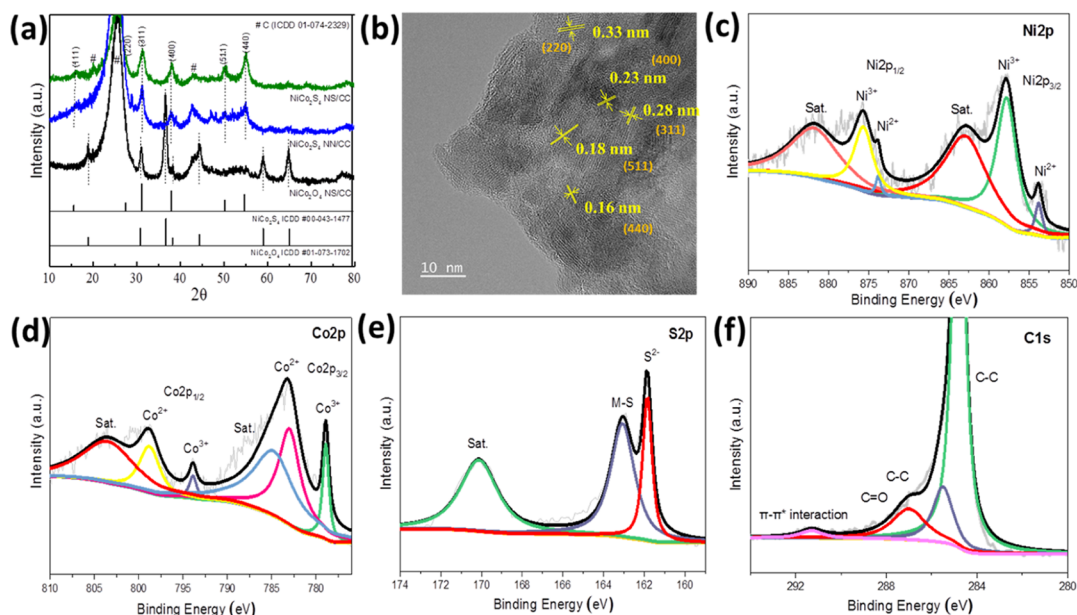


Figure 2. (a) XRD patterns of NiCo₂S₄ NS/CC, NiCo₂S₄ NN/CC, and NiCo₂O₄ NS/CC catalysts. (b) High-resolution TEM images of NiCo₂S₄ NS/CC. High-resolution XPS deconvolution spectra of the NiCo₂S₄ NS/CC catalyst for (c) Ni 2p, (d) Co 2p, (e) S 2p, and (f) C 1s.

morphology perpendicular to a substrate with a rough surface still preserves its architecture (Figure 1e). From the top view of NiCo₂S₄ NS/CC, as shown in Figure 1c,d, the NiCo₂S₄ NSs that are interconnected with each other and form a porous architecture with submicron-size pores, providing ample space for the fast diffusion of redox ions during the reaction, uniformly cover the surface of CC. For comparison, the needle-like shape of NiCo₂S₄ vertically grown on the surface of CC with the average length of 3 μm is also synthesized to understand the effect of morphology on catalytic activities in both alkaline and neutral medium (Figure S2a–c). Also, the NiCo₂O₄ NS/CC was fabricated to have the same morphological characteristics as NiCo₂S₄ NS/CC (Figure S2d–f).

The XRD patterns of NiCo₂S₄ NS/CC, NiCo₂S₄ NN/CC, and NiCo₂O₄ NS/CC are presented in Figure 2a. After oxidation reaction in the first step of the hydrothermal process, nickel–cobalt carbonate hydroxide hydrate NS arrays are uniformly formed on the CC, as shown in Figure S1 (ICDD 00-040-0216). During the sulfurization in the second hydrothermal step, the nickel–cobalt carbonate hydroxide hydrate phase is completely transformed into spinel nickel–cobalt sulfide without destroying the original nanostructures. The diffraction peaks of NiCo₂S₄ NS/CC and NiCo₂S₄ NN/CC at 16.2°, 26.7°, 31.4°, 38.1°, 50.3°, and 55.1° are assigned to the (111), (220), (311), (400), (511), and (440) planes of cubic-phase NiCo₂S₄, respectively (ICDD 00-043-1477). The high-resolution TEM image in Figure 2b reveals the interplanar distance of 0.28, 0.23, 0.16, 0.33, and 0.18 nm, corresponding to the (311), (400), (440), (220), and (511) planes of NiCo₂S₄, respectively, confirming the successful formation of NiCo₂S₄. The formation of NiCo₂S₄ NS/CC is confirmed based on the energy-dispersive X-ray (EDX) using TEM, which shows that the atomic percentages of nickel, cobalt, and sulfur are 15.2, 30.7, and 54.1 at. %, respectively, as shown in Figure S3. Note that the two characteristic peaks at 26° and 43° for all prepared electrodes are attributed to the CC (ICDD 01-074-2329). The diffraction peaks of the NiCo₂O₄ NS/CC catalyst obtained after the first step in the hydrothermal

process and heat treatment are consistent with the standard pattern of NiCo₂O₄ (ICDD 01-073-1702). Meanwhile, the NN-like morphology of NiCo₂S₄ NN/CC can be confirmed from the TEM elemental mapping images shown in Figure S4.

To further characterize the chemical composition of electrodes, the XPS analysis is carried out, and results are given in Figure 2c–f. As shown in Figure 2c, the Ni 2p spectrum consists of two spin–orbit doublets of Ni²⁺ and Ni³⁺, including Ni²⁺ at 853.8 eV for Ni 2p_{3/2} and 873.8 eV for Ni 2p_{1/2}, and Ni³⁺ at 857.7 eV for Ni 2p_{3/2} and 875.6 eV for Ni 2p_{1/2}.^{24,31,35,36} The XPS spectrum of Co 2p (Figure 2d) contains well-resolved peaks of Co²⁺ 2p_{3/2}, Co³⁺ 2p_{3/2}, Co²⁺ 2p_{1/2}, and Co³⁺ 2p_{1/2} at 798.8, 793.9, 783.0, and 778.9 eV, respectively, implying the co-presence of Co²⁺ and Co³⁺ species in NiCo₂S₄ NS/CC.^{23,35} The S 2p XPS spectrum (Figure 2e) shows two peaks at 163.0 and 161.8 eV, which are assigned to metal–sulfur bonds and the low coordination state sulfur ion that exists at the surface of NiCo₂S₄ NS/CC, respectively, with the satellite peak appearing at 170.1 eV in Figure 2e.^{35,36} The C 1s spectrum of NiCo₂S₄ NS/CC is deconvoluted into four peaks located at 284.8, 285.5, 287.0, and 291.3 eV, which correspond to the C 1s orbital of C–C (sp²), C–C (sp), C–O, and π–π interactions, respectively (Figure 2f). The additional π–π interaction indicates the strong interactions between NiCo₂S₄ NSs arrays and the CC, which can minimize contact resistance to generate a direct electron pathway.³⁰ The binding energy values of Ni 2p, Co 2p, and S 2p are matched well with the previous reports on NiCo₂S₄-based materials.

The OER catalytic activity of NiCo₂S₄ NS/CC was first evaluated with a three-electrode setup using a low scan rate of 1 mV s^{−1} to eliminate the capacitive current effects in alkaline solution (1 M KOH, pH = 14). For comparison, NiCo₂S₄ NN/CC, NiCo₂O₄ NS/CC, bare CC, and RuO₂/CC benchmarking OER catalysts were also tested under the same condition. All the synthesized electrodes in this work are directly used as free-standing oxygen-evolving electrodes, including conventional RuO₂/CC, to avoid possible influenc-

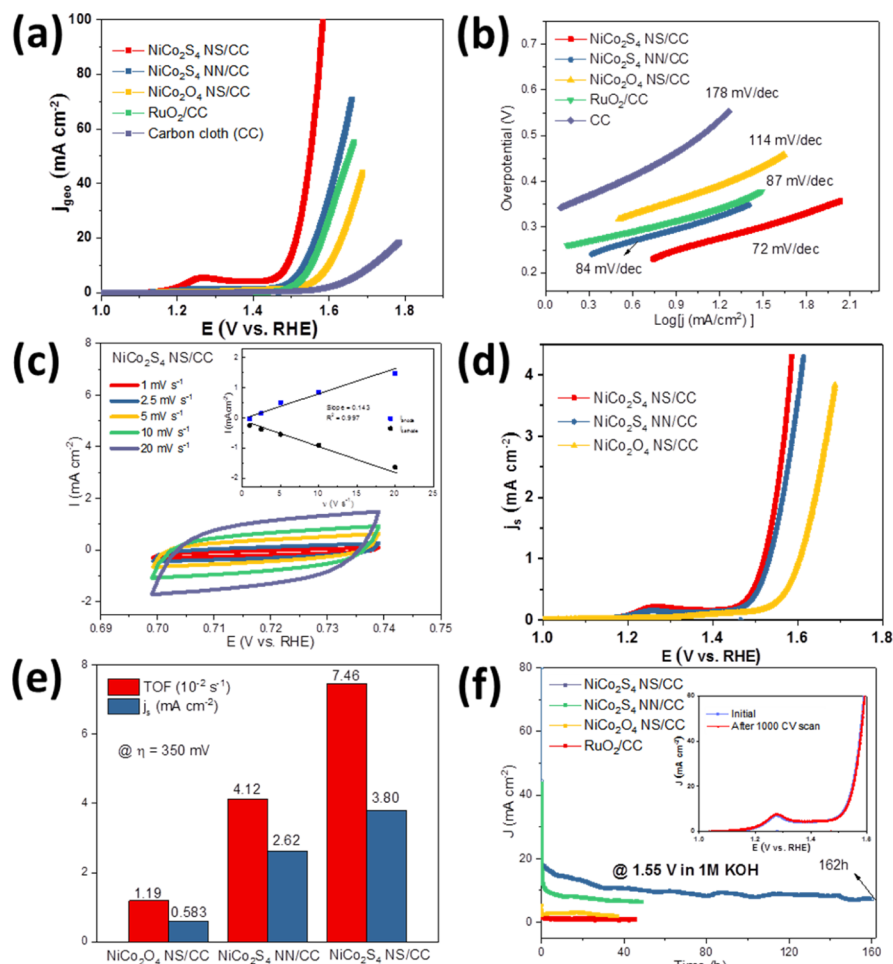


Figure 3. OER in alkaline media (1 M KOH, pH = 14): (a) LSV polarization curves for OER and (b) Tafel plots of NiCo₂S₄ NS/CC, along with NiCo₂S₄ NN/CC, NiCo₂O₄ NS/CC, RuO₂/CC, and CC electrodes for comparison. (c) Cyclic voltammogram measured in a non-faradaic region at various scan rates for the NiCo₂S₄ NS/CC electrode. The inset shows the plot of anodic and cathodic charging current density vs different scan rates. (d) Current density based on intrinsic catalytic activity vs voltage curves. (e) TOF and the specific (intrinsic) activities of NiCo₂S₄ NS/CC, NiCo₂S₄ NN/CC, and NiCo₂O₄ NS/CC electrodes at $\eta = 350$ mV. (f) Time dependence of the current density for NiCo₂S₄ NS/CC at a fixed potential of 1.55 V for 162 h.

ing factors. The LSV polarization curves and Tafel plots for all samples are revealed, as shown in Figure 3a,b. The NiCo₂S₄ NS/CC exhibits a superior catalytic activity toward OER with a low onset potential of only 180 mV. Moreover, the overpotential of 260 mV is required to generate 10 mA cm⁻², which is smaller than that of NiCo₂S₄ NN/CC (316 mV), NiCo₂O₄ NS/CC (368 mV), RuO₂/CC (322 mV), and bare CC (484 mV). Also, it requires only a 280 mV overpotential to afford 10 mA cm⁻² when the scan rate is 5 mV s⁻¹ (Figure S5). It is lower than those of many other reported nonprecious metal-based OER electrocatalysts tested under 1 M KOH conditions, such as NiCo₂S₄ NWs/graphdiyne foam (300 mV), NiCo₂S₄/NF (306 mV)⁻, NiCo₂S₄ NAs/CC (310 mV), and so on.^{22–24,30,32,37–40} A detailed comparison is further summarized in Table S1. The cyclic voltammograms for NiCo₂S₄ NS/CC and NiCo₂O₄ NS/CC in the potential region from 1.0 to 1.8 V show a broad peak at 1.36 and 1.22 V, indicating the redox behavior of Ni²⁺ and Ni³⁺, respectively (Figure S7). The catalytic kinetics of OER is evaluated by Tafel plots in alkaline medium. The Tafel slope of NiCo₂S₄ NS/CC is 72 mV dec⁻¹, which is lower than that of all other electrodes, such as RuO₂/CC (87 mV dec⁻¹), NiCo₂S₄ NN/CC (84 mV dec⁻¹), NiCo₂O₄ NS/CC (114 mV

dec⁻¹), and bare CC (178 mV dec⁻¹), indicating a more favorable rate of OER at the NiCo₂S₄ NS/CC electrode. The favorable kinetics of OER on NiCo₂S₄ NS/CC is also supported by EIS analysis to measure the charge transfer resistance during OER (Figure S6). The charge transfer resistance of NiCo₂S₄ NS/CC, which forms NSs morphology is 8.94 Ω at 1.5 V versus RHE, smaller than that of NiCo₂S₄ NN/CC with NN-like architectures (16.3 Ω). In contrast, NiCo₂O₄ NS/CC shows at least five times higher charge transfer resistance than that of NiCo₂S₄ NS/CC and NiCo₂S₄ NN/CC under the same applied potential because of the lower electrical conductivity of NiCo₂O₄ NS/CC.

To better understand the different OER catalytic activities of NiCo₂S₄ NS/CC, including NiCo₂S₄ NN/CC and NiCo₂O₄ NS/CC catalysts, the ECSA and roughness factor (RF) of all electrodes are determined to estimate the real catalytic activities in the same pH condition. It can be easily calculated based on the double-layer capacitance (C_{dl}) through CV in a non-faradaic region at different scan rates of 1, 2.5, 5, 10, 20, and 50 mV s⁻¹ (Figure 3c). The NiCo₂S₄ NS/CC electrode shows over twofold higher ECSA value of 5.5 mF cm⁻² than that of NiCo₂S₄ NN/CC (2.0 mF cm⁻²) and NiCo₂O₄ NS/CC (2.3 mF cm⁻²), respectively (Figure S8). This indicates that

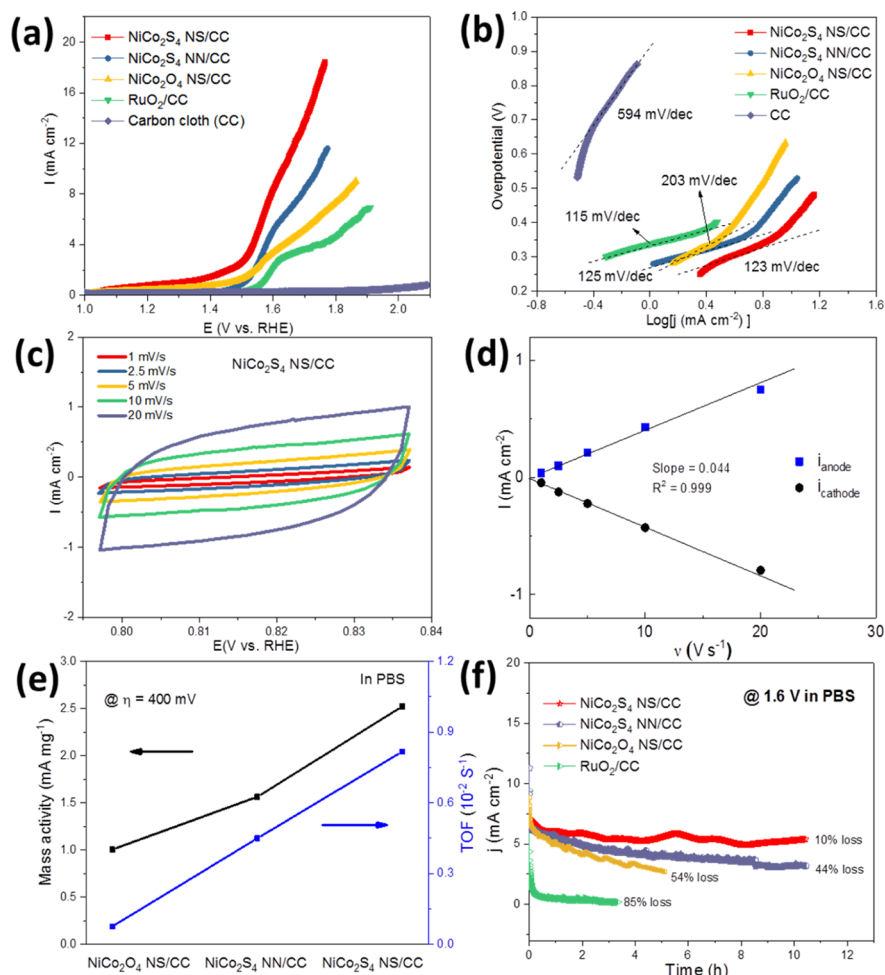


Figure 4. OER in neutral media (phosphate buffer, pH = 7): (a) LSV polarization curves for OER. (b) Corresponding Tafel plots of NiCo₂S₄ NS/CC, along with NiCo₂S₄ NN/CC, NiCo₂O₄ NS/CC, RuO₂/CC, and CC electrodes for comparison. (c) Cyclic voltammogram measured in a non-faradaic region at various scan rates for the NiCo₂S₄ NS/CC electrode. (d) Anodic and cathodic current density vs scan rate plot of NiCo₂S₄ NS/CC. (e) Mass activities and TOF of NiCo₂S₄ NS/CC, NiCo₂S₄ NN/CC, and NiCo₂O₄ NS/CC electrodes in PBS. (f) Time dependence of the current density for NiCo₂S₄ NS/CC at a fixed potential of 1.6 V for 11 h.

plenty of catalytically active sites for OER might form on NiCo₂S₄ NS/CC.

The surface roughness for all electrodes was also calculated by dividing the estimated ECSA to the geometric area of the electrode, and the values of 27.5, 10, and 11.5 were achieved for each electrode, NiCo₂S₄ NS/CC, NiCo₂S₄ NN/CC, and NiCo₂O₄ NS/CC, respectively. On the basis of these results, 2D NS architecture arrays can offer larger space and have a rougher surface; hence, they lead to more electrochemical active sites on the catalyst surface. As a result, the excellent electrocatalytic performances of the NiCo₂S₄ NS/CC electrode can be partially ascribed to the high ECSA and consequently highly exposed active sites.

We further calculate the TOF, which could provide the intrinsic OER catalytic activities of NiCo₂S₄ NS/CC, NiCo₂S₄ NN/CC, and NiCo₂O₄ NS/CC electrodes. The TOF of various electrocatalysts was derived using the following equation:

$$\text{TOF} = \frac{J_{\text{geo}} \times A}{4 \times F \times m}$$

J is the geometric current density at a specific overpotential. A denotes the geometric area of the electrode. The number of

electrons consumed for generating 1 mol of O₂ from water is 4. F is the Faraday constant value of 96 485 C mol⁻¹. m denotes the mole numbers of active materials.⁴¹ On the basis of this calculation, at an overpotential of 350 mV, the TOF of NiCo₂S₄ NS/CC and NiCo₂S₄ NN/CC is calculated as 7.46×10^{-2} and 4.12×10^{-2} mol O₂ s⁻¹, respectively (Figure 3e). In sharp contrast, NiCo₂O₄ NS/CC has the lowest TOF value of 1.19×10^{-2} s⁻¹. Moreover, it is almost fourfold higher than that of the IrO_x catalyst (0.89×10^{-2} s⁻¹), indicating that the NiCo₂S₄ NS/CC is highly efficient toward OER.⁴²

The specific activity of catalysts with different surface areas or loading is calculated with current normalization by the catalyst RF. NiCo₂S₄ NS/CC can deliver a high specific current density of 2.67 mA cm⁻², whereas NiCo₂O₄ NS/CC can produce only 0.96 mA cm⁻² at the same overpotential of 350 mV. Even though their morphology appears to be similar, that is, the density and the distribution of NiCo₂S₄ NSs on the CC are virtually the same as those of NiCo₂O₄ NSs on CC, NiCo₂S₄ NS/CC outperforms NiCo₂O₄ NS/CC. This result shows that NiCo₂S₄ NS arrays on CC have a higher intrinsic OER catalytic activity than that of NiCo₂O₄ NS arrays on CC (Figure 3d), which can be explained by the difference in the crystal structure of NiCo₂S₄ and NiCo₂O₄. NiCo₂S₄ that

formed closely packed arrays of large S^{2-} anions with nickel and cobalt metal cations in different oxidation states occupying the tetrahedral and octahedral sites, respectively, possesses more octahedral active sites of Co(III) concerning $NiCo_2O_4$, which has smaller anions of O^{2-} in the spinel structure.^{32,43} On the basis of the previous literature, σ^* orbital (e_g) occupation-related metal cations at octahedral sites are mostly coordinated with electrocatalytic activities.⁴⁴ In view of this point, $NiCo_2S_4$ NS/CC might afford better OER intrinsic activity compared to $NiCo_2O_4$ NS/CC.

The electrocatalytic activity toward the OER of $NiCo_2S_4$ NS/CC is also evaluated in PBS (pH = 7) as well as control samples as shown in Figure 4a. Similar to the OER activity trend in alkaline media, the $NiCo_2S_4$ NS/CC catalyst exhibits the highest OER performance compared with other electrodes. Surprisingly, $NiCo_2S_4$ NS/CC requires only 321 and 402 mV to afford 5 and 10 mA cm^{-2} , respectively. However, RuO_2/CC as a state-of-the-art OER catalyst needs an extremely large overpotential of 700 mV to deliver 5 mA cm^{-2} current density. At the same time, $NiCo_2S_4$ NN/CC and $NiCo_2O_4$ NS/CC require at least 368 and 460 mV to produce 5 mA cm^{-2} , respectively. Bare CC shows negligible OER performance. The catalytic activity of $NiCo_2S_4$ NS/CC for OER in neutral media is exceptional compared to that of many electrodes reported recently, such as $CoS_{4.6}O_{0.6}$ (η = 570 mV for 5 mA cm^{-2}),¹⁹ ultrathin Co_3S_4 NS (η = 650 mV for 3.27 mA cm^{-2}),⁴¹ Co_3O_4 nanorod (η = 385 mV for 1 mA cm^{-2}),⁴⁵ Co-Pi NA/Ti foam (η = 450 mV for 10 mA cm^{-2}),¹⁵ Co-Bi NSs/graphene (η = 570 mV for 14.4 mA cm^{-2}),¹⁸ and Fe-Ni-P (η = 429 mV for 10 mA cm^{-2}).¹⁴ The detailed comparison is summarized in Table S2. Figure 4b shows the Tafel plots of all electrodes for a better understanding of the obtained catalytic behavior. The Tafel slope of 123 mV dec^{-1} in a neutral electrolyte for $NiCo_2S_4$ NS/CC is achieved. It is the smallest value among $NiCo_2S_4$ NN/CC (125 mV dec^{-1}) and $NiCo_2O_4$ NS/CC (203 mV dec^{-1}) and comparable to that of RuO_2/CC (115 mV dec^{-1}), which in turn favors the kinetics of OER. Notably, in comparison with $NiCo_2O_4$ NS/CC, the $NiCo_2S_4$ NS/CC catalyst presents a lower Tafel slope value, originating from the increase in electrical conductivity as well as more plentiful electrocatalytic active sites correlated with its intrinsic activities.

We further measure the double-layer charging of electrodes via scan-rate-dependent CVs to estimate the effective surface areas for catalytic activity. The potential range in which the non-faradaic region was chosen with the potential window of 0.04 V centered at an open-circuit voltage (OCV) of each system.³⁵ The electrochemical double-layer capacitance for $NiCo_2S_4$ NS/CC is 0.044 mF cm^{-2} , whereas those for $NiCo_2S_4$ NN/CC and $NiCo_2O_4$ NS/CC are 0.025 and 0.023 mF cm^{-2} , respectively, indicating the rougher surface of the $NiCo_2S_4$ NS/CC electrode. It is noticeable that $NiCo_2S_4$ NS/CC still possesses almost twofold higher electrochemical double-layer capacitance than $NiCo_2O_4$ NS/CC in neutral media, which is probably because of the well-aligned hierarchical NSs architecture and the formation of numerous electrochemically active sites. The TOF at the overpotential of 400 mV in neutral media is evaluated to compare the intrinsic activities of $NiCo_2S_4$ NS/CC with those of other comparison electrodes. The calculated TOF for $NiCo_2S_4$ NS/CC is $9.89 \times 10^{-3} s^{-1}$, which is much larger than those for previously reported cobalt-based catalysts, including Co_3S_4 ($1.32 \times 10^{-3} s^{-1}$ at η = 500 mV),⁴¹ Co-Pi ($\sim 2 \times 10^{-3} s^{-1}$ at η = 410 mV),⁴⁶ Co-Bi (1.5

$\times 10^{-3} s^{-1}$ at η = 400 mV),⁴⁷ and Co_3O_4 ($\geq 0.8 \times 10^{-3} s^{-1}$ at η = 414 mV),⁴¹ further suggesting the remarkable OER catalytic activity of $NiCo_2S_4$ NS/CC under neutral conditions. The $NiCo_2S_4$ NN/CC for which $NiCo_2S_4$ NN arrays are grown on CC indicates a TOF of $4.83 \times 10^{-3} s^{-1}$, implying its lower intrinsic activities compared with that of the $NiCo_2S_4$ NS/CC electrode, whereas the TOF of $NiCo_2O_4$ NN/CC is calculated as $2.47 \times 10^{-3} s^{-1}$, which shows the lowest value among the three electrodes. Therefore, the remarkable electrocatalytic activity of $NiCo_2S_4$ NS/CC can partially originate from the higher electrochemical surface area and the direct contact between $NiCo_2S_4$ NS arrays and the CC, which facilitate fast electron transfer as well as enhanced mass transportation. In addition, (i) the intrinsic electrocatalytic activity of the $NiCo_2S_4$ with larger anions compared with $NiCo_2O_4$ so as to expose more cation active sites; (ii) the enough void space among interconnected $NiCo_2S_4$ NSs, which allows facile redox ion diffusion; (iii) the 2D morphology of $NiCo_2S_4$ NSs that yields a large contact area between the catalyst and the electrolyte; and (iv) the formation of the nickel-cobalt (oxy)hydroxide active layer on its surface, which will be discussed later, all contributed to the superb performance of $NiCo_2S_4$ NS/CC in the OER.

The long-term operation of the OER catalyst is a critical issue for practical application. Figure 3f exhibits the chronoamperometric (CA) curve of the $NiCo_2S_4$ NS/CC measured at 1.55 V potential in alkaline media (1 M KOH). After the 29 h CA test, the electrode entirely stabilizes and retains a current density of 10 mA cm^{-2} (without iR corrected) and then is reduced to 85% of its original activity over 160 h long-term operation. The inset of Figure 3f shows the linear polarization curves of $NiCo_2S_4$ NS/CC before and after 1000 CV cycles with 50 mV s^{-1} scan rate and a potential range from 1.2 to 1.7 V. Accordingly, there is no difference in the LSV curve recorded after 1000 CV cycles, indicating its high stability. Meanwhile, we detected losses of larger than 24, 29, and 47% in their current densities within 50 h for $NiCo_2S_4$ NN/CC, $NiCo_2O_4$ NS/CC, and RuO_2/CC , respectively, at the same potential of 1.55 V in 1 M KOH solution. We also performed the durability test for same electrodes under the neutral condition. $NiCo_2S_4$ NS/CC presents excellent durability for 11 h, achieving 6 mA cm^{-2} at 1.6 V versus RHE with only 10% loss. During CA, O_2 gas bubbles were visibly observed from the $NiCo_2S_4$ NS/CC electrode and dissipated quickly into the electrolyte. The $NiCo_2S_4$ NN/CC and $NiCo_2O_4$ NS/CC electrodes show a dramatic catalytic activity loss of 45 and 54%, respectively. Moreover, RuO_2/CC almost lost its catalytic activity after 4 h durability test. The morphological robustness of $NiCo_2S_4$ NS/CC was examined by post-OER FE-SEM analysis under alkaline and neutral conditions (Figure S12). Maintaining morphology with negligible damage is another convincing evidence of the structural robustness of $NiCo_2S_4$ NS/CC observed in the FE-SEM micrographs.

Recently, Li et al.⁴⁷ reported that the nonoxide transition metal-based chalcogenides, especially cobalt selenide catalysts, usually oxidize during the OER under the basic condition and progressively transform to the corresponding TM (oxy)-hydroxides, which is proposed to be the true active species to catalyze the OER.⁴⁸ In the case of the Co_3Se_4/CF electrode, the XPS peak intensity of Se virtually disappears after a 3 h chronopotentiometric electrolysis duration, and after 12 h, Co_3Se_4 is converted to $CoOOH$. Similarly, in our study, we

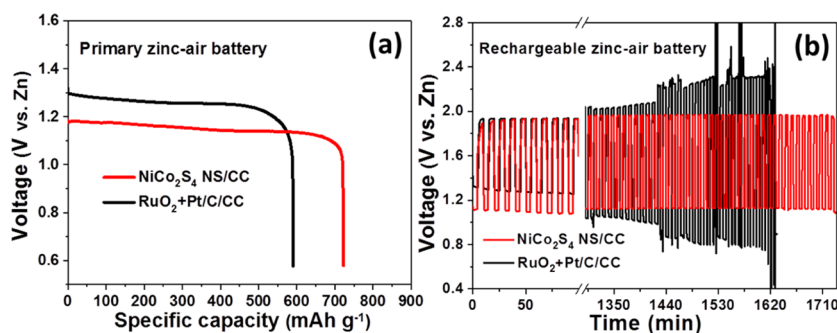


Figure 5. Zn–air battery performance: (a) specific discharge capacities of primary zinc–air batteries with NiCo₂S₄ NS/CC and commercial RuO₂ + Pt/C/CC air cathodes. (b) Comparative galvanostatic charge–discharge profiles of rechargeable zinc–air batteries based on NiCo₂S₄ NS/CC and RuO₂ + Pt/C/CC air cathodes at 5 mA cm⁻² in 10 min interval cycles.

investigated the composition of the electrode after 160 h CA operation by XPS (Figure S11) to confirm the real surface species of NiCo₂S₄ NS/CC. The XPS Ni 2p shows that Ni²⁺ at 853.8 eV for Ni 2p_{3/2} and 873.8 eV for Ni 2p_{1/2} visibly disappears and the peaks located at 855.7 and 873.2 eV are assigned to Ni³⁺ species of the nickel (oxy)hydroxide.^{32,49} Moreover, the binding energy shift of Ni 2p for 1.4 eV reveals the occurrence of electron transfer during extended CA electrolysis. Similarly, the XPS Co 2p_{3/2} peak is deconvoluted into two peaks of 780.7 and 782.3 eV, which represent the formation of Co(OH)₂ and CoOOH, implying the formation of a higher valence state of cobalt (Co³⁺).^{50,51} Meanwhile, the peak intensity of S 2p was weakened, whereas the two strong peaks of O 1s spectra were observed at 531.3 and 532.7 eV, indicating the O–H bond in NiCoOOH and the adsorption of H₂O on the surface of NiCo₂S₄ NS/CC, respectively.^{49–51} The XPS results demonstrate that in situ electrochemical tuning of nickel–cobalt sulfide to nickel–cobalt mixed (oxy)hydroxide phase occurred, which is highly active for the OER catalytic activity attributed to the enhanced surface area and electrochemically active sites. This transformation might change the electronic states and the interactions with intermediate products during OER. Hence, it leads to the catalyst becoming more catalytic active for OER, which is also shown in other chalcogenide materials.^{47,51}

The post-OER durability measurement for over 11 h in the neutral medium was also carried out using XPS analysis to confirm the chemical composition (Figure S12). Similarly, in an alkaline environment, the Ni²⁺ peak disappeared from the surface of catalyzed NiCo₂S₄ NS/CC and transformed to Ni³⁺ of TM (oxy)hydroxides with binding energy values at 855.7 and 873.2 eV as well as satellite peaks at 865.1 and 879.9 eV. Also, the new peaks formed at 779.9 and 781.1 eV are also assigned to the (oxy)hydroxides phase.^{48–51} It is noticeable that similar phenomena of in situ electrochemical tuning for NiCo₂S₄ NS/CC have occurred under a neutral condition, achieving an increase in the surface area as well as electrochemically active sites for primarily improved catalytic activity for OER.

To validate the practical application of the NiCo₂S₄ NS/CC catalyst, a primary zinc–air battery was demonstrated and fully discharged to 0.6 V at a current density of 5 mA cm⁻² (Figure 5a). The NiCo₂S₄ NS/CC cathode shows an OCV of 1.18 V with a specific capacity of 722 mA h g⁻¹, which is almost 88.1% utilization of theoretical capacity (~820 mA h g⁻¹), whereas the commercial catalyst-based cathode shows an OCV of 1.31 V with a discharge capacity of 590 mA h g⁻¹. Moreover, the

galvanostatic discharge–charge cycling performance was evaluated at a current density of 5 mA cm⁻² with a 5 min discharge followed by 5 min charge for each cycle (Figure 5b). For the initial cycle of NiCo₂S₄ NS/CC, the rechargeable battery discharged at 1.11 V versus Zn, with the corresponding charging potential of 1.90 V giving an overall overpotential of 0.79 V, which increased only 0.04 V (1.95 V for charge and 1.12 V for discharge potential) after 30 h battery operation (173 cycles). However, in the case of RuO₂ + Pt/C/CC, the potential gap between charge and discharge increased continuously from 0.61 to 1.00 V even after 1350 min (135 cycles) cycling. The superior cycling durability over 173 cycles with a high discharge capacity of 722 mA h g⁻¹ indicates the excellent electrocatalytic activity and stability of NiCo₂S₄ NS/CC for zinc–air batteries.

A two-electrode alkaline water electrolyzer was developed for full water splitting with NiCo₂S₄ NS/CC and Pt/C/CC as the anode and cathode, respectively, in 1 M KOH solution (Figure 6). To achieve a current density of 10 mA cm⁻², a

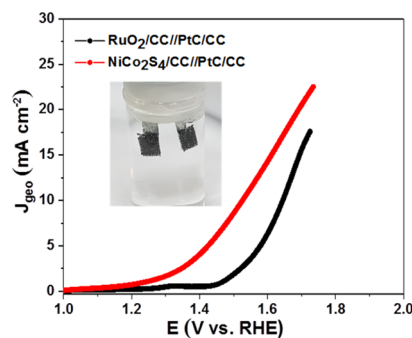


Figure 6. Overall water electrolysis: the polarization curves based on NiCo₂S₄/CC//PtC/CC and commercial RuO₂/CC//PtC/CC electrodes with a scan rate of 5 mV s⁻¹ in 1 M KOH solution. The inset is the photograph of the two-electrode configuration.

voltage of 1.53 V was needed for water splitting with gas evolution on both electrode surfaces, showing more advantages to split water than precious metal-based electrodes, which requires higher cell voltages of 1.64 V.

CONCLUSIONS

In summary, the hierarchical spinel bimetallic sulfide nanostructures in situ grown on the CC were investigated for their electrochemical properties in different pH media and evaluated for their capability in practical primary and

rechargeable zinc–air batteries. The most active NiCo₂S₄ NS/CC electrode can catalyze the OER at an overpotential of 260 mV at 10 mA cm^{−2} with good durability of over 160 h operations under an alkaline condition. Moreover, the NiCo₂S₄ NS/CC electrode still maintained its superior OER catalytic activity under the neutral condition. The enhanced intrinsic catalytic properties, morphology-based advantages of nanostructures, and the generation of the Ni–Co oxyhydroxide active layer were considered responsible for the excellent OER performance in water splitting. Especially, the in situ fabricated NiCo₂S₄ NS/CC-integrated air cathode exhibits excellent durability and electrocatalytic activity in zinc–air batteries compared with the precious metal-based catalyst. This work supports a snapshot of the rational design and construction of nonprecious electrode materials with excellent catalytic activity and durability for the future practical system toward OER in water electrolyzers and zinc–air batteries.

■ ASSOCIATED CONTENT

■ Supporting Information

The Supporting Information is available free of charge on the ACS Publications website at DOI: 10.1021/acsomega.8b01375.

Experimental section; XRD patterns; FE-SEM images; TEM EDX pattern and mapping images; LSV curves; EIS spectra; CV curves measured in the OER region; CV curves and their corresponding charging current density versus different scan rates; postmortem FE-SEM and XPS analysis; and comparison of OER performance with the recently reported literature (PDF)

■ AUTHOR INFORMATION

Corresponding Author

*E-mail: sangarajus@gdist.ac.kr. Phone: +82-53-785-6413 (S.S.).

ORCID

Sangaraju Shanmugam: 0000-0001-6295-2718

Notes

The authors declare no competing financial interest.

■ ACKNOWLEDGMENTS

This work was supported by the DGIST R&D Program of the Ministry of Science, ICT and Future Planning of Korea (18-IT-02), the Korea Institute of Energy Technology Evaluation and Planning (KETEP), and the Ministry of Trade, Industry & Energy (MOTIE) of the Republic of Korea (no. 20174030201590). Additionally, we thank the DGIST-Center for Core Research Facilities (CCRF) for providing various facilities for sample analysis.

■ REFERENCES

- (1) Mallouk, T. E. Divide and conquer. *Nat. Chem.* **2013**, *5*, 362–363.
- (2) Zou, X.; Zhang, Y. Noble metal-free hydrogen evolution catalysts for water splitting. *Chem. Soc. Rev.* **2015**, *44*, 5148–5180.
- (3) Suntivich, J.; May, K. J.; Gasteiger, H. A.; Goodenough, J. B.; Shao-Horn, Y. A perovskite oxide optimized for oxygen evolution catalysis from molecular orbital principles. *Science* **2011**, *334*, 1383–1385.
- (4) Man, I. C.; Su, H.-Y.; Calle-Vallejo, F.; Hansen, H. A.; Martínez, J. I.; Inoglu, N. G.; Kitchin, J.; Jaramillo, T. F.; Nørskov, J. K.

Rossmel, J. Universality in oxygen evolution electrocatalysis on oxide surfaces. *ChemCatChem* **2011**, *3*, 1159–1165.

- (5) Vignesh, A.; Prabu, M.; Shanmugam, S. Porous LaCo_{1-x}Ni_xO_{3-δ} Nanostructures as an Efficient Electrocatalyst for Water Oxidation and for a Zinc-Air Battery. *ACS Appl. Mater. Interfaces* **2016**, *8*, 6019–6031.

- (6) Symes, M. D.; Cronin, L. Materials for Water Splitting. *Materials for a Sustainable Future*; RSC Publishing: Cambridge, UK, 2012; pp 592–614.

- (7) Hao, S.; Yang, Y. Water splitting in near-neutral media: using an Mn-Co-based nanowire array as a complementary electrocatalyst. *J. Mater. Chem. A* **2017**, *5*, 12091–12095.

- (8) Ai, L.; Tian, T.; Jiang, J. Ultrathin Graphene Layers Encapsulating Nickel Nanoparticles Derived Metal-Organic Frameworks for Highly Efficient Electrocatalytic Hydrogen and Oxygen Evolution Reactions. *ACS Sustainable Chem. Eng.* **2017**, *5*, 4771–4777.

- (9) Xu, W.; Lyu, F.; Bai, Y.; Gao, A.; Feng, J.; Cai, Z.; Yin, Y. Porous cobalt oxide nanoplates enriched with oxygen vacancies for oxygen evolution reaction. *Nano Energy* **2018**, *43*, 110–116.

- (10) Zhu, G.; Ge, R.; Qu, F.; Du, G.; Asiri, A. M.; Yao, Y.; Sun, X. In situ surface derivation of an Fe-Co-Bi layer on an Fe-doped Co₃O₄ nanoarray for efficient water oxidation electrocatalysis under near-neutral conditions. *J. Mater. Chem. A* **2017**, *5*, 6388–6392.

- (11) Chen, W.; Liu, Y.; Li, Y.; Sun, J.; Qiu, Y.; Liu, C.; Zhou, G.; Cui, Y. In situ electrochemically derived nanoporous oxides from transition metal dichalcogenides for active oxygen evolution catalysts. *Nano Lett.* **2016**, *16*, 7588–7596.

- (12) Zhou, M.; Weng, Q.; Zhang, X.; Wang, X.; Xue, Y.; Zeng, X.; Bando, Y.; Golberg, D. In situ electrochemical formation of core-shell nickel-iron disulfide and oxyhydroxide heterostructured catalysts for a stable oxygen evolution reaction and the associated mechanisms. *J. Mater. Chem. A* **2017**, *5*, 4335–4342.

- (13) Sivanantham, A.; Shanmugam, S. Nickel selenide supported on nickel foam as an efficient and durable non-precious electrocatalyst for the alkaline water electrolysis. *Appl. Catal., B* **2017**, *203*, 485–493.

- (14) Ganesan, P.; Sivanantham, A.; Shanmugam, S. Inexpensive electrochemical synthesis of nickel iron sulphides on nickel foam: super active and ultra-durable electrocatalysts for alkaline electrolyte membrane water electrolysis. *J. Mater. Chem. A* **2016**, *4*, 16394–16402.

- (15) Zhang, B.; Lui, Y. H.; Ni, H.; Hu, S. Bimetallic (Fe_xNi_{1-x})₂P nanoarrays as exceptionally efficient electrocatalysts for oxygen evolution in alkaline and neutral media. *Nano Energy* **2017**, *38*, 553–560.

- (16) Du, C.; Yang, L.; Yang, F.; Cheng, G.; Luo, W. Nest-like NiCoP for highly efficient overall water splitting. *ACS Catal.* **2017**, *7*, 4131–4137.

- (17) Xie, L.; Zhang, R.; Cui, L.; Liu, D.; Hao, S.; Ma, Y.; Du, G.; Asiri, A. M.; Sun, X. High-performance electrolytic oxygen evolution in neutral media catalyzed by a cobalt phosphate nanoarray. *Angew. Chem.* **2017**, *129*, 1084–1088.

- (18) Lu, Z.; Xu, W.; Zhu, W.; Yang, Q.; Lei, X.; Liu, J.; Li, Y.; Sun, X.; Duan, X. Three-dimensional NiFe layered double hydroxide film for high-efficiency oxygen evolution reaction. *Chem. Commun.* **2014**, *50*, 6479–6482.

- (19) Jiang, J.; Zhang, A.; Li, L.; Ai, L. Nickel-cobalt layered double hydroxide nanosheets as high-performance electrocatalyst for oxygen evolution reaction. *J. Power Sources* **2015**, *278*, 445–451.

- (20) Jiang, J.; Liu, Q.; Zeng, C.; Ai, L. Cobalt/molybdenum carbide@N-doped carbon as a bifunctional electrocatalyst for hydrogen and oxygen evolution reactions. *J. Mater. Chem. A* **2017**, *5*, 16929–16935.

- (21) Chen, P.; Xu, K.; Zhou, T.; Tong, Y.; Wu, J.; Cheng, H.; Lu, X.; Ding, H.; Wu, C.; Xie, Y. Strong-coupled cobalt borate nanosheets/graphene hybrid as electrocatalyst for water oxidation under both alkaline and neutral conditions. *Angew. Chem., Int. Ed.* **2016**, *55*, 2488–2492.

- (22) Cai, P.; Huang, J.; Chen, J.; Wen, Z. Oxygen-Containing Amorphous Cobalt Sulfide Porous Nanocubes as High-Activity Electrocatalysts for the Oxygen Evolution Reaction in an Alkaline/Neutral Medium. *Angew. Chem., Int. Ed.* **2017**, *56*, 4858–4861.
- (23) Liu, J.; Zhu, D.; Ling, T.; Vasileff, A.; Qiao, S.-Z. S-NiFe 2 O 4 ultra-small nanoparticle built nanosheets for efficient water splitting in alkaline and neutral pH. *Nano Energy* **2017**, *40*, 264–273.
- (24) Prabu, M.; Ketpang, K.; Shanmugam, S. Hierarchical nanostructured NiCo₂O₄ as an efficient bifunctional non-precious metal catalyst for rechargeable zinc-air batteries. *Nanoscale* **2014**, *6*, 3173–3181.
- (25) Li, Y.; Zhou, W.; Dong, J.; Luo, Y.; An, P.; Liu, J.; Wu, X.; Xu, G.; Zhang, H.; Zhang, J. Interface engineered in situ anchoring of Co₉S₈ nanoparticles into a multiple doped carbon matrix: highly efficient zinc-air batteries. *Nanoscale* **2018**, *10*, 2649–2657.
- (26) Meng, T.; Qin, J.; Wang, S.; Zhao, D.; Mao, B.; Cao, M. In situ coupling of Co_{0.85}Se and N-doped carbon via one-step selenization of metal–organic frameworks as a trifunctional catalyst for overall water splitting and Zn–air batteries. *J. Mater. Chem. A* **2017**, *5*, 7001–7014.
- (27) Wu, X.; Han, X.; Ma, X.; Zhang, W.; Deng, Y.; Zhong, C.; Hu, W. Morphology-Controllable Synthesis of Zn-Co-Mixed Sulfide Nanostructures on Carbon Fiber Paper Toward Efficient Rechargeable Zinc-Air Batteries and Water Electrolysis. *ACS Appl. Mater. Interfaces* **2017**, *9*, 12574–12583.
- (28) Wang, H.-F.; Tang, C.; Wang, B.; Li, B.-Q.; Zhang, Q. Bifunctional Transition Metal Hydroxysulfides: Room-Temperature Sulfurization and Their Applications in Zn-Air Batteries. *Adv. Mater.* **2017**, *29*, 1702327.
- (29) Xue, Y.; Zuo, Z.; Li, Y.; Liu, H.; Li, Y. Graphdiyne-Supported NiCo₂ S₄ Nanowires: A Highly Active and Stable 3D Bifunctional Electrode Material. *Small* **2017**, *13*, 1700936.
- (30) Miao, J.; Xiao, F.-X.; Yang, H. B.; Khoo, S. Y.; Chen, J.; Fan, Z.; Hsu, Y.-Y.; Chen, H. M.; Zhang, H.; Liu, B. Hierarchical Ni-Mo-S nanosheets on carbon fiber cloth: a flexible electrode for efficient hydrogen generation in neutral electrolyte. *Sci. Adv.* **2015**, *1*, 1500259.
- (31) Sivanantham, A.; Ganesan, P.; Shanmugam, S. Hierarchical NiCo₂S₄Nanowire Arrays Supported on Ni Foam: An Efficient and Durable Bifunctional Electrocatalyst for Oxygen and Hydrogen Evolution Reactions. *Adv. Funct. Mater.* **2016**, *26*, 4661–4672.
- (32) Ma, L.; Hu, Y.; Chen, R.; Zhu, G.; Chen, T.; Lv, H.; Wang, Y.; Liang, J.; Liu, H.; Yan, C.; Zhu, H.; Tie, Z.; Jin, Z.; Liu, J. Self-assembled ultrathin NiCo 2 S 4 nanoflakes grown on Ni foam as high-performance flexible electrodes for hydrogen evolution reaction in alkaline solution. *Nano Energy* **2016**, *24*, 139–147.
- (33) Tian, J.; Liu, Q.; Liang, Y.; Xing, Z.; Asiri, A. M.; Sun, X. FeP Nanoparticles Film Grown on Carbon Cloth: An Ultrahighly Active 3D Hydrogen Evolution Cathode in Both Acidic and Neutral Solutions. *ACS Appl. Mater. Interfaces* **2014**, *6*, 20579–20584.
- (34) McCrory, C. C. L.; Jung, S.; Peters, J. C.; Jaramillo, T. F. Benchmarking heterogeneous electrocatalysts for the oxygen evolution reaction. *J. Am. Chem. Soc.* **2013**, *135*, 16977–16987.
- (35) Sun, M.; Tie, J.; Cheng, G.; Lin, T.; Peng, S.; Deng, F.; Ye, F.; Yu, L. In situ growth of burl-like nickel cobalt sulfide on carbon fibers as high-performance supercapacitors. *J. Mater. Chem. A* **2015**, *3*, 1730–1736.
- (36) Wang, J.-G.; Jin, D.; Zhou, R.; Shen, C.; Xie, K.; Wei, B. One-step synthesis of NiCo 2 S 4 ultrathin nanosheets on conductive substrates as advanced electrodes for high-efficient energy storage. *J. Power Sources* **2016**, *306*, 100–106.
- (37) Liu, D.; Lu, Q.; Luo, Y.; Sun, X.; Asiri, A. M. NiCo₂S₄nanowires array as an efficient bifunctional electrocatalyst for full water splitting with superior activity. *Nanoscale* **2015**, *7*, 15122–15126.
- (38) Li, Y.; Hasin, P.; Wu, Y. Ni₃Co₃–xO₄ Nanowire Arrays for Electrocatalytic Oxygen Evolution. *Adv. Mater.* **2010**, *22*, 1926–1929.
- (39) Liu, J.; Wang, J.; Zhang, B.; Ruan, Y.; Lv, L.; Ji, X.; Xu, K.; Miao, L.; Jiang, J. Hierarchical NiCo₂S₄@NiFe LDH Hetero-structures Supported on Nickel Foam for Enhanced Overall-Water-Splitting Activity. *ACS Appl. Mater. Interfaces* **2017**, *9*, 15364–15372.
- (40) Liu, Y.; Xiao, C.; Lyu, M.; Lin, Y.; Cai, W.; Huang, P.; Tong, W.; Zou, Y.; Xie, Y. Ultrathin Co₃S₄Nanosheets that Synergistically Engineer Spin States and Exposed Polyhedra that Promote Water Oxidation under Neutral Conditions. *Angew. Chem.* **2015**, *127*, 11383–11387.
- (41) Trotochaud, L.; Ranney, J. K.; Williams, K. N.; Boettcher, S. W. Solution-Cast Metal Oxide Thin Film Electrocatalysts for Oxygen Evolution. *J. Am. Chem. Soc.* **2012**, *134*, 17253–17261.
- (42) Zhang, Z.; Wang, X.; Cui, G.; Zhang, A.; Zhou, X.; Xu, H.; Gu, L. NiCo₂S₄ sub-micron spheres: an efficient non-precious metal bifunctional electrocatalyst. *Nanoscale* **2014**, *6*, 3540–3544.
- (43) Suntivich, J.; May, K. J.; Gasteiger, H. A.; Goodenough, J. B.; Shao-Horn, Y. A Perovskite Oxide Optimized for Oxygen Evolution Catalysis from Molecular Orbital Principles. *Science* **2011**, *334*, 1383–1385.
- (44) Ramsundar, R. M.; Debgupta, J.; Pillai, V. K.; Joy, P. A. Co₃O₄ Nanorods-Efficient Non-noble Metal Electrocatalyst for Oxygen Evolution at Neutral pH. *Electrocatalysis* **2015**, *6*, 331–340.
- (45) Surendranath, Y.; Kanan, M. W.; Nocera, D. G. Mechanistic Studies of the Oxygen Evolution Reaction by a Cobalt-Phosphate Catalyst at Neutral pH. *J. Am. Chem. Soc.* **2010**, *132*, 16501–16509.
- (46) Esswein, A. J.; Surendranath, Y.; Reece, S. Y.; Nocera, D. G. Highly active cobalt phosphate and borate based oxygen evolving catalysts operating in neutral and natural waters. *Energy Environ. Sci.* **2011**, *4*, 499–504.
- (47) Li, W.; Gao, X.; Xiong, D.; Wei, F.; Song, W.-G.; Xu, J.; Liu, L. Hydrothermal Synthesis of Monolithic Co₃ Se₄ Nanowire Electrodes for Oxygen Evolution and Overall Water Splitting with High Efficiency and Extraordinary Catalytic Stability. *Adv. Energy Mater.* **2017**, *7*, 1602579.
- (48) Mansour, A. N.; Melendres, C. A. Characterization of Electrochemically Prepared γ -NiOOH by XPS. *Surf. Sci. Spectra* **1994**, *3*, 271–278.
- (49) Yang, J.; Liu, H.; Martens, W. N.; Frost, R. L. Synthesis and characterization of cobalt hydroxide, cobalt oxyhydroxide, and cobalt oxide nanodiscs. *J. Phys. Chem. C* **2010**, *114*, 111–119.
- (50) McIntyre, N. S.; Cook, M. G. X-ray photoelectron studies on some oxides and hydroxides of cobalt, nickel, and copper. *Anal. Chem.* **1975**, *47*, 2208.
- (51) Chen, W.; Wang, H.; Li, Y.; Liu, Y.; Sun, J.; Lee, S.; Lee, J.-S.; Cui, Y. In Situ Electrochemical Oxidation Tuning of Transition Metal Disulfides to Oxides for Enhanced Water Oxidation. *ACS Cent. Sci.* **2015**, *1*, 244–251.